energy&fuels

pubs.acs.org/EF

Article

Effects of Fluid Aging and Reservoir Temperature on Waterflooding in 2.5D Glass Micromodels

Duy Le-Anh,* Ashit Rao, Stefan Schlautmann, Amy Z. Stetten, Subhash C. Ayirala, Mohammed B. Alotaibi, Michel H. G. Duits,* Han Gardeniers, A. A. Yousef, and Frieder Mugele

Cite This: https://doi.org/10.1021/acs.energyfuels.1c03670

Read Online

ACCESS | Metrics & More | Article Recommendations | Supporting Information

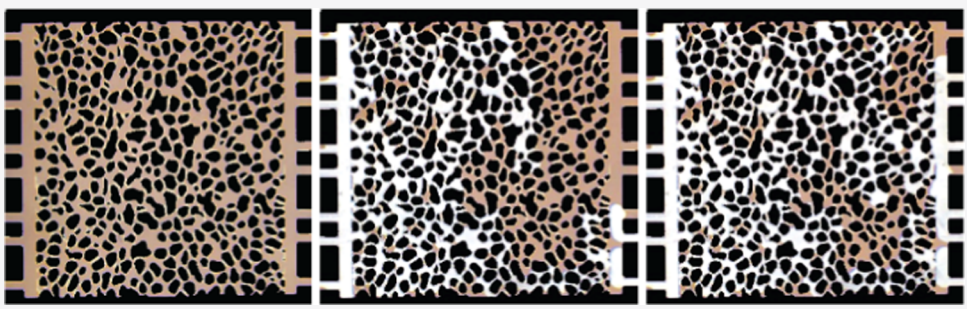

ABSTRACT: To study improved oil recovery (IOR) via laboratory experiments at the pore scale, we performed waterflooding experiments in a glass 2.5D micromodel (dual depth: 12 and 27 μm) with crude oil (CRO) and brines of variable compositions at temperatures ranging from 22 °C (room temperature) to 90 °C. The time-dependent residual oil saturation (ROS) for various flooding and aging protocols was extracted from optical microscopy images of the entire pore space in the micromodel. Additionally, we used high-resolution images to examine the microscopic distributions of oil and brine at the subpore level. Variation of the fluid aging history (before the first flooding with high-salinity water, HSW) revealed that sequential aging with formation water and CRO led to significantly higher ROS values than aging with CRO only. Video analysis of the pore space showed that most of the oil was trapped via a complete bypassing of the deep pores. On increasing the waterflooding temperature, both the ROS and the fraction of bypassed pores became smaller. An increase in dewetting of tiny oil drops and films from the pore walls supports the notion of a ROS decrease via a wettability alteration. Subsequent flooding with low-salinity water (LSW) did not lead to recovery of additional oil, regardless of aging condition or temperature. Our results show the significance of fluid aging and temperature to design a successful microfluidic IOR strategy.

1. INTRODUCTION

A persistent concern on improved oil recovery (IOR) applications is that significant amounts of oil remain trapped in the oil reservoir. In the past decade, low-salinity waterflooding (LSWF)[1] has emerged as a common method to improve oil displacement in both sandstone[2,3] and carbonate[4−8] reservoirs. However, a better comprehensive insight into how LSWF works, as needed to optimize IOR processes, is still lacking.[9]

The use of microfluidics has recently emerged as an alternative, quick, and efficient method to mimic oil recovery.[10,11] In principle, microfluidics can offer quantification of residual oil and microscopic observation of pore scale physical phenomena at a relatively low cost. This is made possible through the broad availability of materials for fabrication (e.g., glass,[12,13] silicon,[14−16] or polymers[17−20]), the low consumption of chemicals, the accurate fluid control and detection, and the flexible design of the pore space.

However, even with these capabilities, the question remains on how to adequately mimic oil recovery processes using the microfluidic platform. IOR processes can present complexity in various ways: (i) the geometry of the pore space,[21,22] (ii) the aging of the rock, brine, and oil (and their interfaces),[23] (iii) the elevated temperature and pressure conditions,[10,24,25] (iv) the complex composition and physicochemical behavior of the crude oil,[26,27] and (v) the fluid/fluid and fluid/rock interactions.[28] Different approaches to this problem have been followed. In reductionistic approaches, simplifications are made using regular pore geometries,[15,29] and/or simple alkanes,[30,31] and/or temperatures around 22 °C.[32,33] Sometimes comparisons to a more complex "reference" experiment are made to validate the simplification.[34,35]

Received: October 27, 2021
Revised: January 5, 2022

In more holistic approaches, certain types of complexities are integrated into the design of the experiment. To better represent the complex structure of the porous rock medium, dual porosity/depth,[36,37] so-called 2.5D[38,39] and 3D micromodels,[40,41] have been used. Also, microfluidic studies at high temperature and pressure have recently seen the light.[42−46] Although the use of crude oil (CRO) in microfluidic devices has been relatively scarce, a growing trend can be observed here.[28,47−49] This has been made possible through the use of chemically resistant chip materials such as glass or silicon. Also, studies on the influence of chemical aging[32] have thereby come within easy reach.

In this paper, we connect to these developments in microfluidic technology to enable mimicking IOR phenomena at higher levels of complexity. Novel explorations are made by addressing two aspects in conjunction: (i) more realistic physicochemical conditions and (ii) a more realistic pore network.

The rich and complex physicochemical behavior of crude oils could play an important role in different stages of the IOR process. Surface-active components (asphaltenes and resins) are known for their ability to adsorb onto rock surfaces as well as brine/CRO interfaces.[50−54] These adsorption (and desorption) behaviors depend on brine composition and temperature and can play distinct roles in wettability alteration during both the initial aging and subsequent waterflooding stages. To examine this aspect, we study the behavior of (nondiluted) crude oil in a glass microfluidic chip at various temperatures. High-temperature aging with CRO is performed with or without a preceding exposure to formation water, which makes a significant difference, as we will show. Subsequent displacement of the CRO by high-salinity water (HSW) is tested as a function of flooding temperature.

Regarding the pore network geometry, a significant influence on the outcome of the waterflooding experiment (e.g., the ROS) could be expected too. Even though comparative studies (e.g., ref 32) using the same physicochemical conditions but different pore network geometries are relatively scarce, it is clear that the pore size (distribution) as well as the pore connectivity must have an effect via the capillary pressures and hydraulic resistances. While microfluidic devices that replicate the 3D nature of the pore network can be made with modern printing technology,[55] the possibility to observe the 3D oil displacement processes with time-resolved (confocal) optical microscopy is precluded by the opaqueness of the crude oil and multilayer structure. Observations are then restricted to the flow channels that are very close to the outer chip surfaces. Possibly in relation to this, many microfluidic studies with CRO are still done in single-depth (i.e., 2D) chips.

Pore spaces characterized by two distinct depths (denoted in the literature as dual depth or 2.5D) do not offer the same pore connectivity as 3D but improve on the 2D systems by better representing the strong variations in pore depth, as well as the stagnant flow regions where oil slugs get trapped more easily. With 2.5D networks, the connectivity between deep and shallow pores can also be better examined for its role in the outcome of IOR processes. Indeed, significant differences in both the ROS and the oil release mechanism have been found for 2D and 2.5D pore networks.[38,39]

To mimic the IOR processes via microfluidic experiments under more realistic conditions, we use a chip with a pore network that closely resembles that of sandstone reservoir rock.[39] The use of glass as the chip material also provides a certain chemical similarity to the sandstone. By etching the pore throats with a shallower depth than the pore bodies, we obtain a 2.5D pore network that offers (i) an approximate representation of the real rock structure (where the pore throats are both narrower and shallower) and (ii) the possibility to optically distinguish between the different types of pores, via the differences in optical path length. In our experiments, optical microscopy is used as the main analysis tool. We first explore the influence of chemical aging, where we will find that exposing the glass pore space to formation water before the standard prolonged exposure to CRO has a significant effect on the ROS values obtained after subsequent waterflooding with HSW. In the second set of experiments, we vary the temperature of the waterflooding from RT to 90 °C and find a clear temperature dependence of the ROS. To obtain more mechanistic insights, we use an image analysis method that first classifies each pore as either deep or shallow and next measures the time-dependent (brine or CRO) content per individual pore. This allows us to elucidate the role of the shallow pores in the fluid displacement pattern. Finally, we use optical microscopy at high magnification to examine for the presence of tiny droplets or thin films in the pores after the waterflooding.

2. MATERIALS AND INSTRUMENTATION

2.1. Fluids. Deionized (DI) water (18.2 MΩ/cm) was obtained from a Millipore Synergy instrument. All chemicals were purchased from Sigma Aldrich. All salts and cleaning agents (ethanol, isopropanol (IPA), toluene, xylene) were used as received. Artificial formation water (FW), high-salinity water (HSW), and low-salinity water (LSW) with ion compositions given in Table S1 (Supporting Information) were prepared by dissolving the salts overnight under stirring at room temperature, followed by filtering through a 0.45 μm polyethersulfone (PES) membrane. LSW is obtained by diluting HSW 10 times. A batch of "dead" crude oil (CRO) was obtained by extracting oil from a reservoir and subsequently removing the dissolved gases and volatile components. The results of a chemical characterization by Saybolt Nederland B.V. are given in Table S2. The viscosities of the CRO at different temperatures as measured with a Haake RS600 rheometer are shown in Table 1. Temperature-dependent interfacial tensions (IFTs) between CRO and brines, measured using a DataPhysics OCA 20L apparatus and inverted pendant drops, are shown in Table 1. The temperatures were chosen as close as possible to those of the flooding experiments (22, 60, and 90 °C) in the microfluidic chip; 85 °C was the highest accessible temperature for the IFT measurement. IFTs between CRO and brine are generally time-dependent; they decrease over the first few minutes and then saturate.[56−58] We present the saturated values measured after 20−25 min.

Table 1. IFT (mN/m) of HSW and LSW with CRO at Different Temperatures[a]

temperature	22 °C	60 °C	85 °C
IFT: HSW and CRO	3.2 ± 0.7	6.7 ± 0.2	7.6 ± 0.4
IFT: LSW and CRO	8.8 ± 0.6	9.5 ± 0.6	10.2 ± 0.5
viscosity: CRO	24	7.4	3.4
viscosity: water	∼1.0	∼0.47	∼0.34

[a]Viscosity (mPa.s) of CRO and water at different temperatures.

2.2. Microfluidic Chips. The design of the entire 2.5D microchannel is shown in Figure 1. Our pore network was inspired by a real sandstone core, as presented in ref 39. In this paper, a cross-sectional scan obtained with micro-computed tomography was subjected to image analysis to separate the pore bodies from the pore throats. After we scaled the pore maps obtained from this paper

https://doi.org/10.1021/acs.energyfuels.1c03670
Energy Fuels XXXX, XXX, XXX−XXX

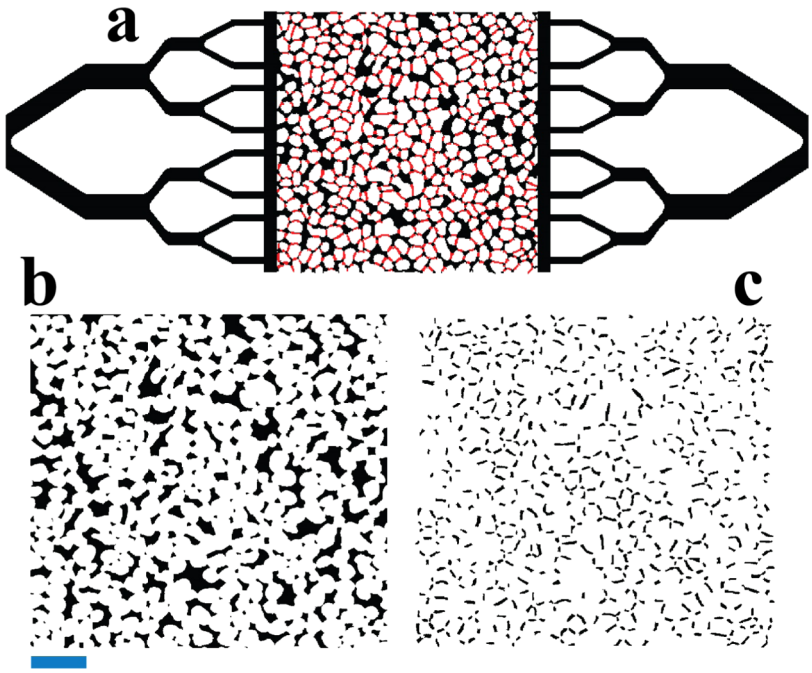

Figure 1. (a) Schematic of the 2.5D micromodel including both the pore network and the distribution fractures. The black regions correspond to deep channels and pores, while the red regions are the shallow pores. Lower panels show the deep (b) and shallow (c) channels separately. Scale bar is 1 mm. Reproduced with permission from ref 39. Copyright [2019] Publisher Elsevier.

to a ∼6.3 mm × 6.3 mm horizontal area, we used them as etch masks. The pore throats were isotropically etched to a depth of 12 μm, while it was 27 μm for the pore bodies. Figure 1b,c shows the deep and shallow pore spaces (projected onto a horizontal plane). The typical lateral dimensions are ∼55 μm for the shallow pores and ∼200 μm for the deep ones (see Figure S1 for the lateral size distributions). Hence, for both pore types, the depth is typically much smaller than the width, implying that the depths will dominate the curvatures of the liquid−liquid interfaces in the chip. Assuming a uniform depth of 27 (12) μm, we calculate a total volume of ∼0.5 (0.09) μL for deep (shallow) pores by multiplying the projected area with the depth. Defining the total volume of the porous medium as 6.3 mm × 6.3 mm × 0.027 mm, we then obtain a porosity of ∼ 55%. Notably, the separate sets of deep and shallow pores do not offer complete flow paths, and hence a sustained transport of fluid can only be realized via alternating flow through deep and shallow pores.

The lithography process used for etching the dual-depth pore space in a glass wafer is discussed in the Supporting Information. The obtained etched glass substrate was bonded to a 100 mm diameter 200 μm thick glass MEMpax substrate in which circular holes (∼2 mm diameter) had been powder blasted (abrasive jet machined).[59] These holes served as the inlet and the outlet for the liquids. After thermally bonding the wafers, the wafer pair was diced into five individual chips. Finally, a ∼20 nm chromium layer was sputtered on the backside of the glass chip to enhance the reflectivity for the impinging light of the upright optical microscope onto which the chip was mounted (see Figure S3).

Experiments at elevated temperatures were made possible via a homemade chip holder (Figure S4) that was made from PEEK because of its chemical inertness and good thermal insulation. Temperature control over the chip was achieved by attaching it to a (high thermal conductivity) copper block, which in turn was attached to a ceramic heater (HT24S 24W, Thorlabs). A TCS651 thermistor was placed inside the copper block (see Figure S5), and both the heater and the thermistor were connected to a 5300 TEC Source temperature controller. The typical temperature difference across the pore space of the chip was measured to be as small as ∼0.5 °C.

Teflon tubings (1.6 mm OD × 0.5 mm ID) were connected to the inlets of the glass chip via Viton O-rings, PFA (Teflon)/ETFE 1/4″-28 UNF thread fitting, and ETFE Ferrules 1/4″-28. The inlet tubing and syringe were connected via male 1/4″-28 threaded fittings and a male Luer lock adapter. Liquids were injected using a syringe pump (KD Scientific) and a 1 mL gastight glass syringe (Hamilton).

2.3. On-Chip Measurements. All aging and waterflooding experiments were carried out with the micromodels embedded in the holder (held at a constant temperature) that was placed on the stage of a Zeiss Axioskop upright microscope equipped with a Basler (type a2A5328-15ucBAS) 5328 × 4608 pixels color CCD camera (see Figure S3). Using a 2× objective allowed us to capture the entire pore space in a single projection image (∼1.6 μm/pixel). Using this magnification, movies at a frame rate of 30/s were collected by capturing from a virtual monitor screen of 644 × 562 pixels using Active Presenter recording software (∼11.4 μm/pixel). An independent 10× objective was used to acquire high-resolution still images (∼0.32 μm/pixel) of selected pores.

The absolute permeability of the 2.5D microchannel was measured by injecting DI water and increasing the pressure stepwise from 400 to 1800 mbar using an OB1 Mk3+ controller (Elveflow). The corresponding flow rates were measured using a mini-Cori M12 flowmeter (Bronkhorst). The permeability K was calculated by linear fitting to Darcy's Law[60]

$$K = \frac{Q\mu L}{A\Delta P} \tag{1}$$

where Q is the injection flow rate, μ is the viscosity of water, ΔP is the pressure drop, and A the cross-sectional area of the channel. The data shown in Figure S6 confirm the laminar nature of the flow (maximum Reynolds number ∼ 1) and give a value of ∼1.6 Darcy. The permeability of our micromodel is within the range of sandstone cores.[61]

2.4. Aging and Waterflooding Protocols. With aging, we mean the set of chemical exposures of the pore space prior to the waterflooding. The aging starts with clean glass and ends with an (almost) completely CRO-filled chip at room temperature (RT). Examined aging conditions were as follows: (i) no aging, (ii) CRO aging, and (iii) subsequent FW and CRO aging. In aging conditions (ii) and (iii), the chip was filled with the aging liquid(s) at RT, heated up to 95 °C (at a rate of 5 °C/min), held at that temperature for a certain time, and then cooled down to RT. The dwell time was 1.5 h

https://doi.org/10.1021/acs.energyfuels.1c03670
Energy Fuels XXXX, XXX, XXX−XXX

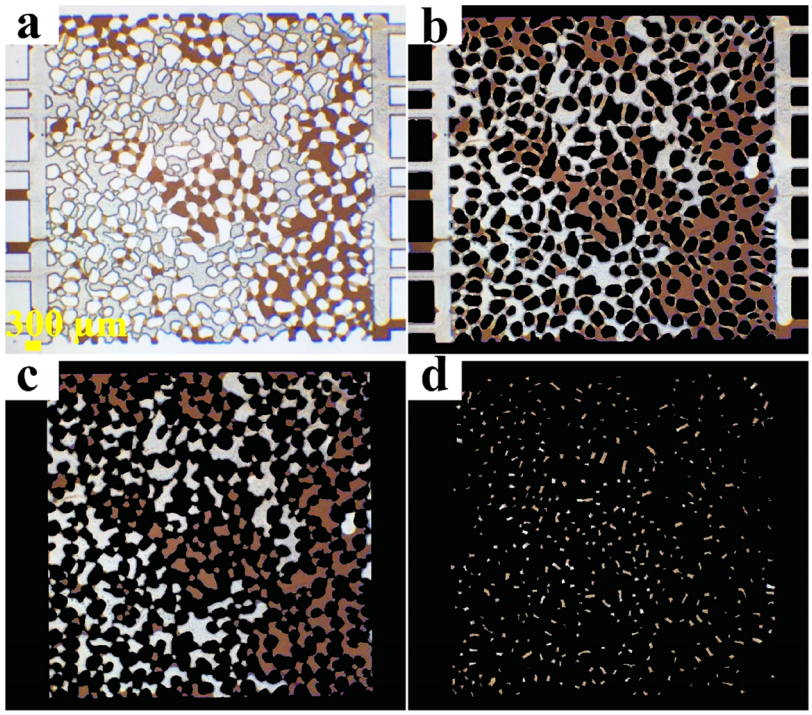

Figure 2. (a) Example of an original micromodel image after waterflooding; (b) glass parts are filtered out to reveal only fluid pores and (c) deep and (d) shallow pores are further separated.

for FW and 22 h for CRO, to take into account the fact that CRO molecules need more time to adsorb than ions from the FW. The deposition of CRO molecules on glass slides under these conditions was confirmed by confocal Raman microscopy (not shown). Fillings and displacements were performed at a rate of 0.2 μL/min. The filling with FW was preceded by flushing with ethanol to avoid trapping of air bubbles; after that, 10 pore volumes (PVs) of FW were pumped through the chip to ensure complete removal of the ethanol. The injection with CRO at 0.2 μL/min was sustained during the 22 h dwell time. Next, subsequent injections of HSW and LSW were carried out at 0.2 μL/min for 30 min (corresponding to 10 PV) and 60 min (20 PV), respectively. This similar flooding timescale was also used in other studies[32,48] and was sufficient to remove a significant fraction of the trapped oil. Based on our measurements of the interfacial tensions and viscosities of our system (Table 1), we find that the capillary number ranges between $\sim 6 \times 10^{-6}$ and $\sim 8 \times 10^{-7}$, indicating that capillary forces must play an important role at all temperatures and brine compositions.[62,63] In practical IOR, the typical superficial injection velocity is up to 4 ft/day in traditional core floods.[64] Ours is comparable to $\sim$ 5.2 ft/day.

All waterflooding experiments were preceded by a 30 min waiting time to ensure thermal equilibration of the chip. Flooding temperatures were maintained constant at either 22 °C, 60 °C, or 90 °C. After the waterflooding experiments, the micromodels were cleaned to enable reuse. After flushing with 1 mL of toluene and 1 mL of xylene + IPA (50/50% vol) to remove organics, they were injected with abundant amounts of DI water and dried under air flow. A final heating step in an oven at 500 °C was done to remove any organic traces.[32]

3. IMAGE ANALYSIS

3.1. Separation between Glass, Shallow Pores, and Deep Pores. A flowchart of the principal image analysis steps is shown in Figure S7. Most image analyses were performed on video data of the entire pore space captured at a 644 × 562 pixel resolution. To enhance visualization and to facilitate quantitative analysis, the porous medium was divided into glass, deep pores, and shallow pores. This separation was achieved by analyzing the colors (i.e., RGB pixel values) in a high-resolution (5328 × 4608 pixels) "reference image" of a chip that had been completely filled with CRO. In the first RGB thresholding step, the glass parts were identified, and the corresponding pixels turned black (R = 0, G = 0, B = 0). This step is illustrated in Figure S8. Setting the same pixels to (000) in each subsequent video image during the waterflooding resulted in better visualization of the brine invasion pattern.

The remaining non-black pixels were also further subjected to color thresholding, making use of the stronger light absorption of the CRO in the deep pores, compared to the shallow ones (see Figure S8). While this second thresholding yielded "deep pore" and "shallow pore" maps that closely resembled the mask images shown in Figure 1b and c, it also resulted in some artifacts, like individual pixels that were incorrectly assigned to deep or shallow pores and pores that appeared connected, whereas they should be separated based on the etch mask design (and the etching conditions). These issues were resolved via Matlab-based erosion/dilation and object-filling operations. The so-improved pore space images were then transformed into (high-resolution) binary masks. A subtle difference between these masks and the etch masks is that the transition zones between the two pore depths are more easily "cloven" into deep/shallow via the RGB colors.

Since the pore space was identical for all used chips, the same high-resolution masks were used in all experiments. However, before these masks could be applied, it had to be taken into account that (i) the video images had a lower pixel resolution and (ii) mounting the chip into the holder never resulted in exactly the same position. Therefore, for each new experiment, a video image of the CRO-filled chip before waterflooding was compared to the high-resolution "reference image" using Matlab's MSER image registration method. The obtained transformation matrix was then used to properly scale down and align the two reference masks onto the video images.

https://doi.org/10.1021/acs.energyfuels.1c03670
Energy Fuels XXXX, XXX, XXX−XXX

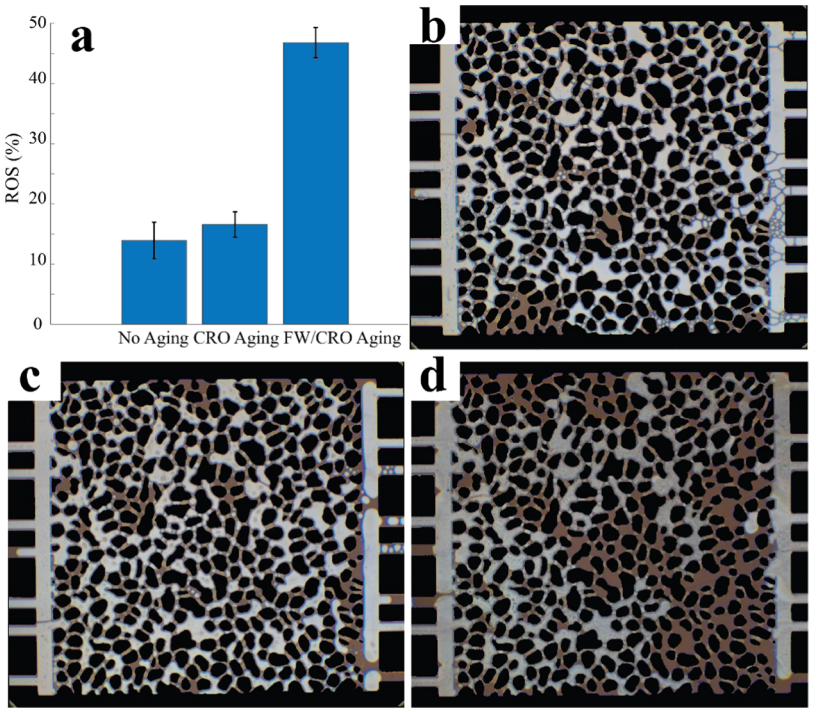

Figure 3. Influence of aging protocol on the outcome of subsequent waterflooding with HSW at room temperature. (a) Residual oil saturation values are displayed with error bars (standard deviation) from three experiments per aging condition. See text for further details. Illustrative images of the corresponding brine/CRO distributions: (b) no aging, (c) aging with CRO, and (d) subsequent aging with FW and CRO.

As illustrated in Figure 2, these filtering operations allow the generation of separate color maps for deep (Figure 2c) and shallow (Figure 2d) pore spaces. Brine invasion of both pore types is visible via local color changes. To calculate the residual oil saturation (ROS) for each pore subspace (deep or shallow), each pixel belonging to that subspace was assigned a status of either being brine-filled or CRO-filled based on the grayscale value (after conversion from RGB values). Threshold gray levels were based on the histograms at the beginning (fully oil-saturated) and at the end (partially brine-saturated) of the experiment. ROS values of the deep and shallow pore spaces were then calculated by simply counting the numbers of brine- and CRO-assigned pixels of the involved pore subspace.

The ROS of the entire pore space was calculated from the ROS values of the subspaces as a weighted average, where the weight factor of each subspace was given by the product of the number of pixels and the (12 or 27 μm) pore depth. Here, it is worth noting that the shallow pores correspond only to about 10% of the total pore volume.

3.2. Tracking Changes in Individual Pores. Using the masks for the "deep" and "shallow" pore spaces, a more detailed analysis was also carried out. Utilizing the lack of connectivity between pores within the same subset, each individual pore was given a unique identifier that was stored along with the (x,y) pixel locations occupied by the pore. This separation allowed us to analyze the time dependence of the liquid content of each individual pore.

Two types of signals were calculated. First, the evolution of the average grayscale value of each pore (corresponding to ROS) was smoothened with a Savitzky−Golay filter and subsequently differentiated with respect to time.

$$S_1(t) = \mathrm{SGF}\left(\frac{1}{N}\sum_{i=1}^{N} \mathrm{GR}_i^{t+1} - \mathrm{GR}_i^{t}\right) \quad (2)$$

where SGF indicates the noise filtering, i is the pixel index, N is the number of pixels of the considered pore, t is the video frame number, and GR indicates the grayscale value. The $S_1(t)$ signal allows detection of brine invasion through a peak (see Figures S9 and S10).

Second, RGB color difference images between two subsequent video frames were transformed into a mean square difference per pixel

$$S_2(t) = \frac{1}{N}\sum_{i=1}^{N} \{(\mathrm{R}_i^{t+1} - \mathrm{R}_i^{t})^2 + (\mathrm{G}_i^{t+1} - \mathrm{G}_i^{t})^2 + (\mathrm{B}_i^{t+1} - \mathrm{B}_i^{t})^2\} \quad (3)$$

where i, N, and t have the same meaning as before, and R, G, and B indicate the corresponding color channels. Signal $S_2(t)$ not only detects events like progressive brine invasion but also changes that leave the average grayscale unaltered, such as the motion of a trapped brine droplet within a pore, which produces a nonzero $S_2(t)$, unlike $S_1(t)$, which would remain (near) zero. The normalization of $S_1(t)$ and $S_2(t)$ by the number of pixels produces numbers that can be compared between differently sized pores. This is useful for distinguishing peaks from random noise.

4. RESULTS

4.1. Influence of Aging Conditions on Residual Oil Saturation. The residual oil saturation (ROS) values obtained after executing the different (high temperature) aging protocols and subsequently flooding with 10 pore volumes of HSW (at room temperature) are shown in Figure 2. Clearly, the aging procedure has a significant effect on the outcome of the subsequent waterflooding. Leaving out the aging, i.e., starting the waterflooding after filling the pristine chip with CRO (and waiting 30 min, see Section 2.4), results in an oil

https://doi.org/10.1021/acs.energyfuels.1c03670
Energy Fuels XXXX, XXX, XXX−XXX

retention of 13%. Aging the pore space with CRO at 95 °C for 22 h before the RT waterflooding leads to a ROS of 17%. The strongest effect is, however, observed when the CRO aging is preceded by exposure to FW; this leads to a ROS of 46%. Illustrative images of the brine/CRO-filled pore spaces after the HSW flooding are shown in Figure 3 for different aging protocols. Remarkably, following up the HSW flooding by ~20 PVs of low-salinity water (LSW) does not lead to any noticeable change in the ROS in our experiments. An interpretation of these trends is given in Section 5. Considering that the combined FW/CRO aging protocol is the most representative of mimicking in situ reservoir conditions, we will focus the remainder of this paper on experiments with this aging condition.

4.2. Locations of Oil Retention. Focusing on the HSW flooding experiment after FW/CRO aging, we can obtain additional insights from an analysis of the dynamic distribution of the brine and oil. Time-resolved analysis of the video images allows us to monitor the evolution of the residual oil saturation. As shown in Figure 3, saturation of the ROS is already reached after about 1 pore volume, suggesting that no further changes occur after the first sweep. A similar finding (saturation after 1−2 PVs) was reported in a recent study with 2D glass micromodel.[32]

Distinguishing between deep and shallow pores (see Section 3.2) allows us to calculate separate ROS values (shown in Figure 4). As might be expected from the observed

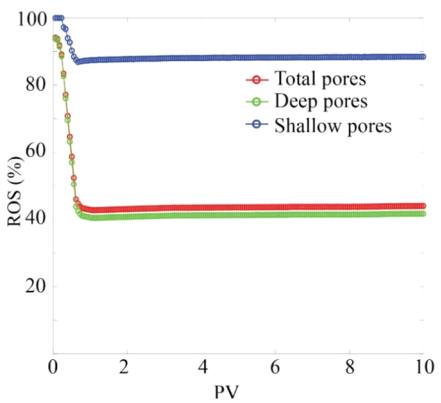

Figure 4. Evolution of residual oil saturation as a function of the number of injected HSW pore volumes (1 PV ~ 0.6 μL). The ROS is dominated by the contribution of the deep pores. Both the deep and shallow pore subsets reach saturation after about 1 PV (corresponding to about 3 min). The ROS values for the deep and shallow pores are relative to the total volume of the respective pore type.

homogeneous spread of both pore subspaces over the 6.3 mm × 6.3 mm area (see Figure 1), both ROS values for deep and shallow pores reach their steady values roughly simultaneously. Notably, the ROS of the shallow pores is significantly higher than the ROS of the deep pores. While the direct effect hereof on the total oil retention is modest because shallow pores only occupy ~0.1 PV, there is also an indirect and more important effect as we will see.

To obtain more insight into the relation between CRO release and the 2.5D pore network structure, we now consider the pattern of the brine invasion. To achieve this, we analyzed the time-dependent brine/oil distribution for each individual pore. After calculating the signals $S_1(t)$ and $S_2(t)$ from eqs 2 and 3, they were compared with corresponding noise levels T_1 and T_2 (measured during the waterflooding, during the stage that the pores had not been invaded with brine). Owing to the occurrence of pronounced peaks in $S_1(t)$ and $S_2(t)$ for a large number of pores, T_1 and T_2 could be defined from the average magnitudes of the same $S(t)$ signals prior to the appearance of the first peak (we remind the reader that both $S_1(t)$ and $S_2(t)$ should be zero in the absence of brine/CRO redistribution). Subsequent use of these T_1 and T_2 values to define thresholds enabled us to detect which pores got invaded with brine and at what time. More details on this can be found in the Supporting Information (Figures S9 and S10).

The occurrence of the first peak in $S_1(t)$ and $S_2(t)$ thus indicates when the first brine invasion takes place for the considered pore. Thus, knowing the "opening times" for each of the pores, we made a reconstructed video in which each pore was given a uniform color to indicate whether or not it had been previously invaded by brine. Using green for invaded and red for noninvaded pores (lighter shades were used for the shallow pores) produces Video S1 in the Supporting Information.

Figure 5a shows a single frame from that video taken at the end of the HSW flooding stage (at 10 PV). Dark and light brown-colored pores were never invaded by brine. Considering how the noninvaded (i.e., CRO-filled) deep pores are connected to the shallow pores, it becomes evident from Figure 5a that shallow pores can act as "gatekeepers" for the deep ones. A significant fraction of the deep pores (the ones shown as dark brown) turns out to be completely bypassed by the flowing brine due to blocking shallow "gateways" (indicated with light brown). For the shown experiment, this mechanism is responsible for 71% of the residual oil. An interpretation will be given in Section 5.

This also means that 29% of the residual CRO is retained via another mechanism, i.e., trapping in pores that got invaded by the brine but did not completely get "cleared" by it. This is illustrated (for the deep pores only) in Figure 5b; the pores that were completely filled with dark green in Figure 5a (because they were invaded) now show the internal distributions of both brine (light green) and oil (yellow). Analysis of the $S_2(t)$ signals indicates that these distributions are generally stable. This could mean (i) that the entire pore gets bypassed by the brine flow from a certain point in time or (ii) that the pore still participates in the flow network, but the flowing brine is unable to change the spatial distribution of the brine and the CRO in the pores. While, in principle, we cannot distinguish between the two scenarios (particle image velocimetry experiments would be required for that), indications can be found for both. Some pores show a large brine/CRO interface in the central region, which could be in agreement with scenario (i). Other pores show accumulation of CRO near the side walls in possible agreement with scenario (ii). Although it cannot be concluded from Figure 5b, it is also conceivable that the dual-depth nature of the pore network could contribute to scenario (ii) by providing "dead ends" in the vertical direction.

Finally, we use still images made at increased microscope magnification (10×) and maximum image resolution (5328 × 4608 pixels) to reveal additional details of the state obtained after the HSW flooding. As illustrated in Figure 6, it turns out that the brine-invaded pores do not only contain large oil slugs as shown in Figure 5b but also much smaller droplets and films of CRO. On comparing the color intensity of the small droplets with that of CRO-filled pores (all deep pores have the

https://doi.org/10.1021/acs.energyfuels.1c03670
Energy Fuels XXXX, XXX, XXX−XXX

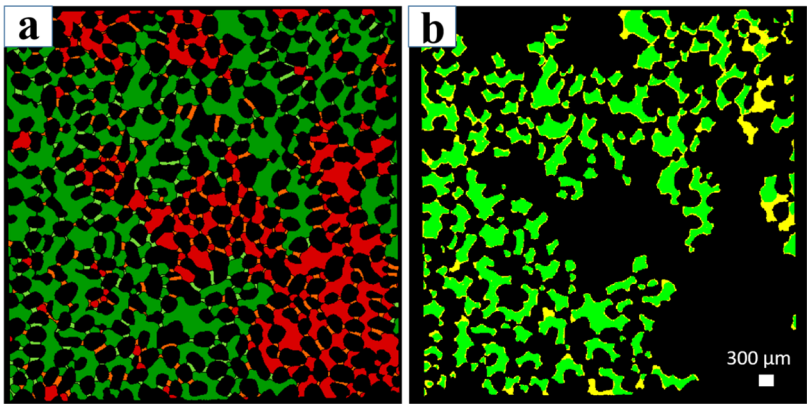

Figure 5. Reconstructions of pore space on the FW/CRO-aged chip after HSW flooding at room temperature. Both images correspond to the steady state after ≫1 PV. (a) History plot in which colors indicate whether the pore has previously been invaded by the brine (bright green or dark green) or not (red or orange). (b) Invaded deep pore space. Colors indicate for each individual pixel whether it is filled with brine (green) or oil (yellow).

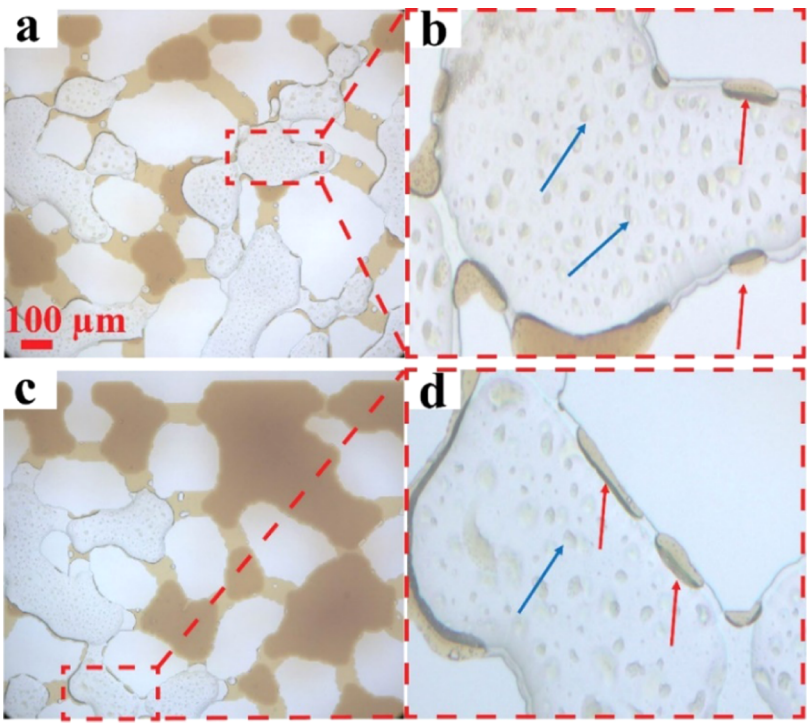

Figure 6. Representative high-resolution images of pores invaded by HSW after aging in FW/CRO at 95 °C and subsequent flooding with HSW at room temperature. (a) and (c) correspond to different samples of the pore space. (b) and (d) are magnified regions of the pictures on the left. Blue arrows indicate CRO droplets, while red arrows indicate CRO films.

same height and hence the same optical path length), we infer that the small droplets are not spanning the 27 μm local pore height but instead are attached to either the floor (or ceiling) and have brine above (or below) them. The adherence of the CRO films or slugs to the side walls is likely a manifestation of the same interaction between FW/CRO-aged and subsequently HSW-exposed glass and crude oil.

These finer details also shed some light on the classification of individual pixels as either brine- or CRO-filled; this classification seems to depend on the optical resolution, and ROS values might get underestimated by classifying pores, as shown in Figure 5b, as 100% brine-filled. However, these slight inaccuracies should not affect any of our main conclusions.

4.3. Influence of the Waterflooding Temperature. Adhering to the FW/CRO aging protocol, we next explore the influence of the flooding temperature. Figure 7 summarizes the results for the residual oil saturation. A clear trend is observed; ROS decreases with temperature upon flushing with high-salinity (i.e., HSW) brine. For example, the waterflooding at RT presents a ROS of 46%, whereas it is 36% for flooding at 90 °C. Representative pore spaces after HSW flooding at different temperatures are shown in Figure S11. Similar to our observations at RT, no significant changes in ROS were found at elevated temperatures after changing to LSW as the flooding fluid.

Next, we turn to the more detailed quantitative analysis of the locations of CRO retention, as discussed and illustrated for the RT waterflooding in Section 4.2. Table 2 provides an overview of the different oil retentions for three typical experiments at 22, 60, and 90 °C. The first column shows the

https://doi.org/10.1021/acs.energyfuels.1c03670
Energy Fuels XXXX, XXX, XXX−XXX

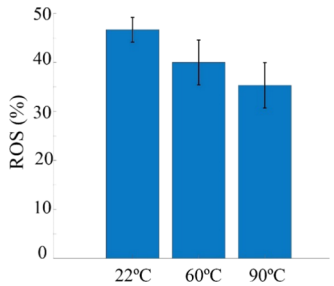

Figure 7. ROS of HSW injection at different temperatures in glass channels that were aged in FW and CRO at (95 °C). The ROS decreases with waterflooding temperature. Error bars indicate the standard deviation from three experiments per condition.

Table 2. Dependence of Residual Oil Saturation on the Pore Type and Waterflooding Temperature

pore type and temperature	ROS	bypassed pores	invaded pores
shallow at 22 °C	0.83	0.62	0.20
shallow at 60 °C	0.76	0.51	0.24
shallow at 90 °C	0.54	0.35	0.19
deep at 22 °C	0.45	0.32	0.13
deep at 60 °C	0.41	0.21	0.20
deep at 90 °C	0.37	0.14	0.22

ROS values per subset: all shallow pores or all deep pores. At all temperatures, the shallow pores have a higher proportion of residual CRO after the flooding. Meanwhile, the ROS in the shallow pores follows the same decreasing trend with temperature as in the deep pores. The second and third columns show how the residual CRO is divided between the pores that are completely bypassed and the pores that get brine-invaded but still retain CRO (refer to Figure 5b). If a higher waterflooding temperature is chosen, the amount of oil that remains behind due to complete bypassing of deep pores clearly becomes smaller (second column). In other words, at higher temperatures, it is easier to "open up" the deep pores. However, the deep pores that do get invaded retain the oil more effectively at higher temperatures (third column). The dominant mechanism of CRO retention thus changes with temperature.

Lastly, we also extend our visual inspection of the pore space (as done in Figure 6) to higher waterflooding temperatures. From a comparison of the brine-invaded pores in Figure 8, it can be seen that the tiny CRO drops embedded in the brine as observed at RT are also found at 60 and 90 °C, albeit these droplets appear to have become smaller and less abundant (especially at 90 °C). Focusing on the pores that are mostly filled with crude oil, another trend can be observed; for higher temperatures, the CRO slugs get increasingly separated from the pore walls by rather thick brine layers (this is most clearly visible from Figure 8c, corresponding to 90 °C).

To extract more quantitative information about this "dewetting" phenomenon, we examined the whole pore spaces and calculated the fraction of edges that showed this "dewetting." Here, we define an edge as an interface between the remaining CRO in a pore and one of the glass grains that defines the pore. Figure 8d displays the "dewetting fraction" defined above as a function of flooding temperature. However, at room temperature, this dewetting is insignificant; only a slight dewetting is measured at 60 °C, and at 90 °C, the dewetting fraction reaches as high as 36%.

We like to point out here that the brine layers indicative of the dewetting were not observed during the high-temperature (95 °C) aging. Since this aging with CRO was preceded by exposure to FW (see Section 2.4), brine layers wetting the

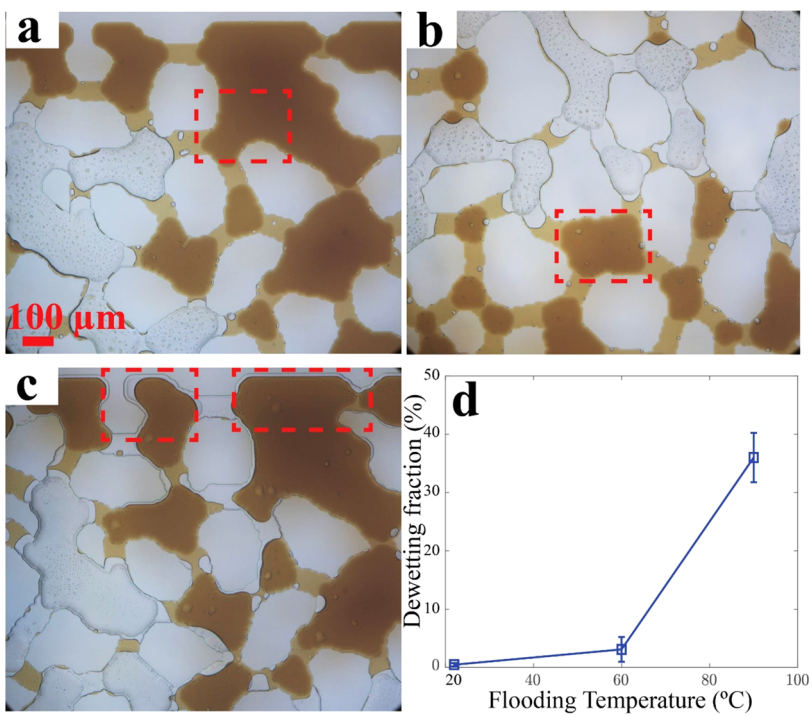

Figure 8. Representative pore scale images after HSW flooding at different temperatures: (a) RT, (b) 60 °C, and (c) 90 °C. (d) Dewetting fraction at three different temperatures for HSW flooding. Error bars indicate the standard deviation measured from three experiments. See text for details on the calculation. The glass areas were not marked black in this figure to better visualize the glass walls.

https://doi.org/10.1021/acs.energyfuels.1c03670
Energy Fuels XXXX, XXX, XXX−XXX

glass walls may have been present during the aging step. However, in spite of the high temperature, they were not thick enough to be visible. This indicates that the appearance of thick brine layers during the waterflooding at 90 °C is not simply the consequence of a thermal expansion of water films that were present already during the aging. The implication hereof is that additional brine must have been flowing into the pores during the waterflooding. Most likely, "gutter flows" were responsible for this.

5. UNDERLYING PHYSICOCHEMICAL ASPECTS

5.1. Liquid Invasion Pattern. The outcome of waterflooding experiments at the level of the retention fraction (i.e., residual saturation) of the defending liquid is the resultant of an interplay between (at least) hydraulic and capillary pressures. In porous networks, this interplay becomes complex because of (i) the fluid-mechanical coupling between the pores and (ii) the changes in the global pressure drop (between the inlet and the outlet of the pore network) as the invading fluid advances. The ensuing pattern by which the pore space is filled by the invading fluid also determines the amount of defending fluid that is retained.

Because of the complex collective behavior of the pores, quantitative predictions of how the retention fraction depends on flow rate, interfacial tensions, viscosities, and pore dimensions can only be made via numerical calculations.[65] In the so-called "moving capacitor" model,[66] the pore space is represented by an equivalent electrical network in which capillary menisci act as capacitors and differences in wettability (i.e., contact angle) function as batteries. These concepts were also used in a recent modeling study,[67] which extends the well-known work of Lenormand et al.[68] via a systematic variation of the contact angle. Using circular posts to define a network of relatively shallow pores (Hele-Shaw) at a constant height (2D geometry), Primkulov et al. calculated a "phase diagram" for the filling pattern as a function of three parameters: capillary number, viscosity ratio, and contact angle. Hysteresis in the contact angle was not taken into account.

Disregarding the differences between their used pore geometry and our 2.5D network, a crude comparison between Primkulov's predictions and our experiments can still be made. The phase diagram (see Figure 12 in ref 67) has three axes: capillary number (Ca), viscosity ratio (M), and the contact angle of the invading phase (Θ). Based on measurements of the temperature-dependent interfacial tensions and viscosities of our system, we find that our viscosity ratio varies from ∼0.05 to ∼0.1, while our (standard) capillary number ranges between $\sim 6 \times 10^{-6}$ and $\sim 8 \times 10^{-7}$ (see Table 3) for the temperature range of 22−85 °C. For these typical numbers, the theoretical phase diagram (shown in Figure S13) shows a transition in the filling pattern from "invasion percolation" toward "cooperative filling" as Θ decreases. The more compact displacement pattern observed at elevated temperatures (Figure S11) could therefore be in agreement with a wettability alteration of the glass surfaces toward a water-wet state, as was already suggested by the observations in Figure 8.

Table 3. Capillary Number (Ca) of HSW and LSW Injection and Viscosity Ratio in Our Waterflooding Experiments at Different Temperatures[a]

	22 °C	60 °C	85 °C
Ca (HSW)	6.1×10^{-6}	1.4×10^{-6}	8.7×10^{-7}
Ca (LSW)	2.2×10^{-6}	9.6×10^{-7}	6.5×10^{-7}
viscosity ratio	∼0.04	∼0.06	∼0.1

[a] $Ca = \mu v/\gamma$ with $v = 1.8 \times 10^{-5}$ m/s. $M = \mu_{inv}/\mu_{def}$ with the brine as the invading phase.

5.2. Pore Yielding. In another interpretative approach, we can make some simplifying assumptions for the (time-dependent) pressure distribution in the pore network while taking into account the distinction between deep and shallow pores. Taking a closer look at the geometries of both types of pores, it is clear that generally (i) all pores have a width that is much bigger than their height (shown in Figure S1) and (ii) the shallow pores also have a smaller width than the deep pores (see Figures 1 and S1). This means that for the shallow pores, both the capillary pressure threshold (in the case the flow is blocked) and the hydraulic resistance (in the case the flow is permitted) will be significantly larger.

In our experiments, changes take place during injection of the first pore volume of brine (see Figure 4 and SI Video S2). Until the point that the brine has reached the back end of the pore space, a gradually increasing number of menisci have to yield, causing the pressure drop over the entire chip (and hence also over the pore space) to increase. However, upon reaching "water breakthrough," a low-resistance flow path is created, leading to a steep decrease in the overall pressure drop (for example, ref 32). Assuming a similarly shaped transient pressure drop for our system, several of the observations can be explained.

Considering the pores to be slit-like (width ≫ height) with a height h (being either 12 or 27 μm) and the contact angle of the CRO to be Θ_{CRO}[a], a simplistic yield criterion can be formulated for each pore. The brine/CRO interface will get displaced if

$$\Delta P > \frac{2\gamma}{h}\cos \Theta_{CRO} \tag{4}$$

where γ is the brine/CRO interfacial tension and ΔP is the pressure drop across the pore (with brine at the front end and CRO at the back end). Before the "breakthrough," i.e., the point where the flow of the brine has reached the back end of the pore network, the liquid displacement imposed by the pump will ensure that some local pressures will get high enough to enforce progressive brine invasion of the pore space. After the breakthrough, the local pressures in the pore network will be determined by the local flow rates, hydraulic resistances, and capillary yield pressures, similar to the currents, resistors, and capacitors in an electric network.[66,67] If the hydraulic resistances in the "breakthrough flow path" of the brine are large enough, then the local pressure drops over some till-then noninvaded pores can still exceed the yielding pressure, leading to new brine invasions. Additional flow paths created in this way will further lower the hydraulic resistance until the point is reached where all local pressure drops are too low to satisfy eq 4. The brine flow pattern then stabilizes, leaving the pores that are still filled with CRO intact. This explains why the ROS reaches saturation of about 1 PV (similar to other studies[32,39]).

It is also clear from eq 4 that (for all $\Theta_{CRO} < 90°$) the shallow pores will offer stronger resistance to capillary yielding. This could explain our finding that the ROS is always higher in the shallow pores (Figure 4). An indirect consequence of the pore connectivity in our 2.5D micromodel is that the deep pores can only be reached via shallow pores. This means that effectively the brine invasions are governed by capillary

https://doi.org/10.1021/acs.energyfuels.1c03670
Energy Fuels XXXX, XXX, XXX−XXX

yielding of the shallow pores. This is also what we observe in Figure 5a.

The same simplistic picture can also explain why the secondary flooding with LSW does not produce any changes in the brine/CRO distribution. As shown in Table 1, the interfacial tensions of the LSW with the CRO are always higher than those of the HSW, meaning that the capillary yielding pressures of the remaining brine/CRO menisci only get higher, while the hydraulic pressures due to the brine flow remain essentially the same (considering that the flow rates are the same and the viscosity should be slightly lower for the LSW).

Lastly, we consider how raising the waterflooding temperature affects the balance between hydraulic and capillary pressures. As shown by Table 1, all fluids show a clear decrease in viscosity, meaning that for the same flow rate, the hydraulic pressures will be much smaller. In contrast, the brine/CRO interfacial tensions show an increase. Looking at eq 4, the changes in ΔP and γ would work together in making it more difficult for the flow to invade the pores. However, our experiments show the opposite trend since the ROS decreases with temperature (Figure 7). This suggests that the more abundant yielding of the pores at elevated temperatures would be due to a significant increase in Θ_{CRO}, or, in other words, a wettability alteration toward a water-wet state.

5.3. Molecular Origin of Wettability Alteration. This important role of wettability directs toward the discussion of the two key trends found in this work (Figures 3a and 7) from the microscopic point of view, i.e., the adsorption and desorption of CRO molecules on the glass surfaces.

The trend in Figure 3a implies that FW/CRO aging renders the glass surface in a more oil-wet state than aging with CRO only. This perhaps counterintuitive finding is, however, plausible; a clear wettability alteration of clean glass can only originate from the adsorption of CRO molecules. Crude oil contains many surface-active components (e.g., asphaltenes, resins) having both hydrophilic and hydrophobic sides. Adsorption of their hydrophilic sides onto the glass, stimulated by divalent cations from the FW, could thus expose the hydrophobic sides to the pore space. This behavior is also well known for fatty acids in mica[69−71] and oxidized silicon[72] substrates and crude oil on quartz substrates[73,74] and calcite substrates[75,76] at room temperature and elevated temperatures. Asphaltene adsorption on glass surfaces has also been reported in the literature.[77−79]

The clear decrease in ROS we observed at elevated waterflooding temperatures (Figure 7) would be consistent with a wettability alteration toward a water-wet state, via an increased desorption of amphiphilic CRO molecules at higher temperatures. It is well known that both the aggregation and the adsorption of asphaltenes are highly temperature-dependent (e.g., ref 80 and references therein), making it unsurprising that temperature would have an effect on the desorption as well. Strong wettability alteration via the effect of temperature on interfacial assembly has also been found for model systems like mica surfaces and fatty acids.[81]

6. COMPARISON TO OTHER STUDIES

Considering the various other microfluidic and core flooding studies done in recent years with the aim to better understand improved oil recovery and given the multitude of variables that can influence the residual oil saturation, it is interesting and relevant to compare the outcomes of other studies with a similar scope.

Several other studies aimed at mimicking recovery processes with micromodels have also used glass to define the pore space.[32,46,48] While it is clear that the surface composition of glass is significantly simpler than that of reservoir rock, glass is considered in many microfluidic and millifluidic studies to be "chemically similar" to sandstone rock. Both glass and sandstone present silicon dioxide groups at the surface, and in sandstone reservoirs that contain little clay,[82] SiO_2 is by far the most abundant mineral species.

Remarkably, only a few microfluidic studies using glass devices have examined the influence of the chemical aging history. Exposure of the micromodel to CRO for a certain waiting time prior to the waterflooding is common to all aging protocols, but it has been done with[32] and without a preceding exposure to FW. Different aging temperatures have also been used. Comparisons between these different aging protocols are scarce. In a recent study by Saadat et al., different aging protocols were compared using 2D glass chips with a regular pore structure. They also found a significant increase in ROS if the aging in CRO was preceded by an aging step in brine.[32] The same work also found a very modest increase in oil recovery after a second flooding with lower salinity brine; in our case, the effect was too small to measure within the accuracy of our method. These similar trends seem to confirm the important role of wettability alteration, which should indeed depend on the materials' chemistry rather than the pore network geometry.

Also, the influence of the waterflooding temperature on CRO recovery has not been addressed much in other experimental studies using glass micromodels. Again, the qualitative trends in the ROS can be expected to depend on the materials rather than the geometry. The finding in a recent study[46] that different CROs with distinct SARA/TAN profiles produced qualitatively different temperature dependences of ROS underlines this point. Numerical simulations, even if performed in simple 2D pore networks[83] could play an important role in mapping these varying experimental outcomes onto model parameters.

Dewetting phenomena, whether induced by chemical aging, brine salinity, or temperature, also fit well into the scope of microfluidic studies. Since its manifestation depends on the underlying physicochemical processes, both the required (temperature, pressure, composition) conditions and the timescale at which it manifests can vary widely. For example, Mahzari et al.[84] found dewetting after low-salinity flooding at ∼206 bar and 60 °C. Bartels et al.[29] observed incipient oil dewetting during high-salinity flooding at RT but only after a long time (several days). The stark contrast with our study, where a timescale of minutes was sufficient to generate the dewetting films, underlines the need to obtain a better insight into the underlying physicochemical processes.

Another important aspect in the development of microfluidic devices to study oil recovery processes is the geometry of the pore network. Recent work shows an increased interest in the connectivity or dimensionality (2D, 2.5D) of the pore space.[38,39] While such geometrical aspects at the micron scale do not influence the molecular processes that change the interfacial tensions and wettability, the consequences of the pore space geometry for the quantitative oil mobilization efficiency can be significant.[39] The present work, in which the shallow pores are identified as the gatekeeper for the brine

https://doi.org/10.1021/acs.energyfuels.1c03670
Energy Fuels XXXX, XXX, XXX−XXX

invasion of the deep pores, also confirms the important role of the pore space geometry.

These ongoing developments of the microfluidic platform as a tool to better understand and optimize conditions for IOR are promising in the sense that already some trends, as found in core flooding experiments, can be reproduced.[85−88] However, it is also clear that some phenomena occurring in the real rock reservoirs could only be replicated via more sophisticated micromodels. One example could be the introduction of clay particles adsorbed onto the pore walls; these particles could change the outcome of the IOR process via desorption or swelling.[89,90] Also, the sandstone rock itself may need to be better mimicked. Glass materials as used in the current fabrication of micromodels cannot represent aspects like heterogeneity, swelling, or dissolution.[32,46,48]

7. CONCLUSIONS

Microfluidics is a powerful tool for the study of improved oil recovery (IOR) from rock reservoirs via laboratory experiments at the pore scale. We used microfluidic technology to fabricate a pore network that was made from glass and with a structure that was inspired by sandstone rock. This structure, showing a network of shallow and deep pores where no path across the chip exists without both depths, was translated into a so-called 2.5D microfluidic device using two different etch depths. By performing waterflooding experiments, we extracted time-dependent residual oil saturation (ROS) data for variable brine composition, aging protocol, and temperature. Both aging protocol and temperature showed a pronounced effect on ROS in microfluidic IOR. The video images revealed complex behavior where shallow pores acted as "gatekeepers" to deeper pores, and entire regions of the chip remained oil-filled at long times due to an inability for the shallow "gates" to be forced open. This behavior can be explained through comparison to 2D models of Laplace pressure and hydraulic resistance in pores of variable size. Additionally, high-resolution images of the waterflooding process revealed visible changes in wettability in which CRO gets dewetted from pore walls and a change in CRO retention mechanism at elevated temperatures. This understanding should lead to a more complete picture of oil mobilization mechanisms in 3D pore networks at representative reservoir conditions.

■ ASSOCIATED CONTENT

Supporting Information

The Supporting Information is available free of charge at https://pubs.acs.org/doi/10.1021/acs.energyfuels.1c03670.

Table of the composition of brines, CRO properties, pore size distribution, the fabrication process of a microchannel, experimental setup, image analysis of pore space, detection of pore invasion event, phase diagram (PDF)

Dynamic pore status: invaded or not (AVI)

Brine invasion till steady state (AVI)

■ AUTHOR INFORMATION

Corresponding Authors

Duy Le-Anh − *Physics of Complex Fluids, MESA+ Institute, Faculty of Science and Technology, University of Twente, 7500 AE Enschede, The Netherlands;* orcid.org/0000-0002-3254-9028; Email: a.d.le@utwente.nl

Michel H. G. Duits − *Physics of Complex Fluids, MESA+ Institute, Faculty of Science and Technology, University of Twente, 7500 AE Enschede, The Netherlands;* orcid.org/0000-0003-1412-4955; Email: m.h.g.duits@utwente.nl

Authors

Ashit Rao − *Physics of Complex Fluids, MESA+ Institute, Faculty of Science and Technology, University of Twente, 7500 AE Enschede, The Netherlands;* orcid.org/0000-0002-5440-8007

Stefan Schlautmann − *Mesoscale Chemical Systems groups, MESA+ Institute, Faculty of Science and Technology, University of Twente, 7500 AE Enschede, The Netherlands*

Amy Z. Stetten − *Physics of Complex Fluids, MESA+ Institute, Faculty of Science and Technology, University of Twente, 7500 AE Enschede, The Netherlands*

Subhash C. Ayirala − *The Exploration and Petroleum Engineering Center—Advanced Research Center (EXPEC ARC), Saudi Aramco, Dhahran 34465, Saudi Arabia*

Mohammed B. Alotaibi − *The Exploration and Petroleum Engineering Center—Advanced Research Center (EXPEC ARC), Saudi Aramco, Dhahran 34465, Saudi Arabia*

Han Gardeniers − *Mesoscale Chemical Systems groups, MESA + Institute, Faculty of Science and Technology, University of Twente, 7500 AE Enschede, The Netherlands;* orcid.org/0000-0003-0581-2668

A. A. Yousef − *The Exploration and Petroleum Engineering Center—Advanced Research Center (EXPEC ARC), Saudi Aramco, Dhahran 34465, Saudi Arabia*

Frieder Mugele − *Physics of Complex Fluids, MESA+ Institute, Faculty of Science and Technology, University of Twente, 7500 AE Enschede, The Netherlands;* orcid.org/0000-0003-3824-3617

Complete contact information is available at: https://pubs.acs.org/10.1021/acs.energyfuels.1c03670

Notes

The authors declare no competing financial interest.

■ ACKNOWLEDGMENTS

The authors thank Daniel Wijnperlé for assisting with the microscope setup and N. Schilderink for measuring IFT of crude oil and brines.

■ ADDITIONAL NOTE

[a]It is remarked here that more precisely, Θ_{CRO} should be the receding contact angle, which will be smaller than Young's angle. However, since we only consider relative changes in contact angle, we will ignore the difference.

■ REFERENCES

(1) Bernard, G. G. In *Effect of Floodwater Salinity on Recovery of Oil from Cores Containing Clays*, SPE California Regional Meeting; OnePetro, 1967.

(2) Morrow, N.; Buckley, J. Improved oil recovery by low-salinity waterflooding. *J. Pet. Technol.* **2011**, *63*, 106−112.

(3) Tang, G.-Q.; Morrow, N. R. Influence of brine composition and fines migration on crude oil/brine/rock interactions and oil recovery. *J. Pet. Sci. Eng.* **1999**, *24*, 99−111.

(4) Gupta, R.; Smith, G. G.; Hu, L.; Willingham, T.; Lo Cascio, M.; Shyeh, J. J.; Harris, C. R. In *Enhanced Waterflood for Carbonate Reservoirs-Impact of Injection Water Composition*, SPE Middle East Oil and Gas Show and Conference; Society of Petroleum Engineers, 2011.

(5) Yousef, A. A.; Al-Saleh, S.; Al-Kaabi, A.; Al-Jawfi, M. Laboratory investigation of the impact of injection-water salinity and ionic content on oil recovery from carbonate reservoirs. *SPE Reservoir Eval. Eng.* **2011**, *14*, 578−593.
(6) Shehata, A. M.; Alotaibi, M. B.; Nasr-El-Din, H. A. Waterflooding in carbonate reservoirs: Does the salinity matter? *SPE Reservoir Eval. Eng.* **2014**, *17*, 304−313.
(7) Nasralla, R. A.; Sergienko, E.; Masalmeh, S. K.; van der Linde, H. A.; Brussee, N. J.; Mahani, H.; Suijkerbuijk, B. M.; Al-Qarshubi, I. S. Potential of low-salinity waterflood to improve oil recovery in carbonates: Demonstrating the effect by qualitative coreflood. *SPE J.* **2016**, *21*, 1643−1654.
(8) Nasralla, R. A.; Mahani, H.; van der Linde, H. A.; Marcelis, F. H.; Masalmeh, S. K.; Sergienko, E.; Brussee, N. J.; Pieterse, S. G.; Basu, S. Low salinity waterflooding for a carbonate reservoir: Experimental evaluation and numerical interpretation. *J. Pet. Sci. Eng.* **2018**, *164*, 640−654.
(9) Bartels, W.-B.; Mahani, H.; Berg, S.; Hassanizadeh, S. Literature review of low salinity waterflooding from a length and time scale perspective. *Fuel* **2019**, *236*, 338−353.
(10) Lifton, V. A. Microfluidics: an enabling screening technology for enhanced oil recovery (EOR). *Lab Chip* **2016**, *16*, 1777−1796.
(11) Cao, S. C.; Jung, J.; Radonjic, M. Application of microfluidic pore models for flow, transport, and reaction in geological porous media: from a single test bed to multifunction real-time analysis tool. *Microsyst. Technol.* **2019**, *25*, 4035−4052.
(12) Grate, J. W.; Kelly, R. T.; Suter, J.; Anheier, N. C. Silicon-on-glass pore network micromodels with oxygen-sensing fluorophore films for chemical imaging and defined spatial structure. *Lab Chip* **2012**, *12*, 4796−4801.
(13) Karadimitriou, N. K.; Joekar-Niasar, V.; Hassanizadeh, S. M.; Kleingeld, P. J.; Pyrak-Nolte, L. J. A novel deep reactive ion etched (DRIE) glass micro-model for two-phase flow experiments. *Lab Chip* **2012**, *12*, 3413−3418.
(14) Gunda, N. S. K.; Bera, B.; Karadimitriou, N. K.; Mitra, S. K.; Hassanizadeh, S. M. Reservoir-on-a-Chip (ROC): A new paradigm in reservoir engineering. *Lab Chip* **2011**, *11*, 3785−3792.
(15) Grate, J. W.; Warner, M. G.; Pittman, J. W.; Dehoff, K. J.; Wietsma, T. W.; Zhang, C.; Oostrom, M. Silane modification of glass and silica surfaces to obtain equally oil-wet surfaces in glass-covered silicon micromodel applications. *Water Resour. Res.* **2013**, *49*, 4724−4729.
(16) Song, W.; Kovscek, A. R. Functionalization of micromodels with kaolinite for investigation of low salinity oil-recovery processes. *Lab Chip* **2015**, *15*, 3314−3325.
(17) Berejnov, V.; Djilali, N.; Sinton, D. Lab-on-chip methodologies for the study of transport in porous media: energy applications. *Lab Chip* **2008**, *8*, 689−693.
(18) Sollier, E.; Murray, C.; Maoddi, P.; Di Carlo, D. Rapid prototyping polymers for microfluidic devices and high pressure injections. *Lab Chip* **2011**, *11*, 3752−3765.
(19) Ma, K.; Liontas, R.; Conn, C. A.; Hirasaki, G. J.; Biswal, S. L. Visualization of improved sweep with foam in heterogeneous porous media using microfluidics. *Soft Matter* **2012**, *8*, 10669−10675.
(20) Wu, C. Y.; Owsley, K.; Di Carlo, D. Rapid software-based design and optical transient liquid molding of microparticles. *Adv. Mater.* **2015**, *27*, 7970−7978.
(21) Anbari, A.; Chien, H. T.; Datta, S. S.; Deng, W.; Weitz, D. A.; Fan, J. Microfluidic model porous media: fabrication and applications. *Small* **2018**, *14*, No. 1703575.
(22) Gogoi, S.; Gogoi, S. B. Review on microfluidic studies for EOR application. *J. Pet. Explor. Prod. Technol.* **2019**, *9*, 2263−2277.
(23) Ramanathan, R.; Shehata, A.; Nasr-El-Din, H. *Effect of Rock Aging on Oil Recovery during Water-Alternating-CO2 Injection Process: An Interfacial Tension, Contact Angle, Coreflood, and CT Scan Study*, SPE Improved Oil Recovery Conference; OnePetro, 2016.
(24) Sharma, G.; Mohanty, K. K. Wettability alteration in high-temperature and high-salinity carbonate reservoirs. *SPE J.* **2013**, *18*, 646−655.
(25) Lu, J.; Goudarzi, A.; Chen, P.; Kim, D. H.; Delshad, M.; Mohanty, K. K.; Sepehrnoori, K.; Weerasooriya, U. P.; Pope, G. A. Enhanced oil recovery from high-temperature, high-salinity naturally fractured carbonate reservoirs by surfactant flood. *J. Pet. Sci. Eng.* **2014**, *124*, 122−131.
(26) Fjelde, I.; Omekeh, A. V.; Sokama-Neuyam, Y. A. *Low Salinity Water Flooding: Effect of Crude Oil Composition*, SPE Improved Oil Recovery Symposium; OnePetro, 2014.
(27) McMillan, M. D.; Rahnema, H.; Romiluy, J.; Kitty, F. J. Effect of exposure time and crude oil composition on low-salinity water flooding. *Fuel* **2016**, *185*, 263−272.
(28) Siadatifar, S. E.; Fatemi, M.; Masihi, M. Pore scale visualization of fluid-fluid and rock-fluid interactions during low-salinity waterflooding in carbonate and sandstone representing micromodels. *J. Pet. Sci. Eng.* **2021**, *198*, No. 108156.
(29) Bartels, W.-B.; Mahani, H.; Berg, S.; Menezes, R.; van der Hoeven, J. A.; Fadili, A. Oil configuration under high-salinity and low-salinity conditions at pore scale: a parametric investigation by use of a single-channel micromodel. *SPE J.* **2017**, *22*, 1362−1373.
(30) AlDousary, S. *Determining Pore Level Mechanisms of Alkaline Surfactant Polymer Flooding Using a Micromodel*, SPE Annual Technical Conference and Exhibition; OnePetro, 2012.
(31) Vavra, E.; Puerto, M.; Biswal, S. L.; Hirasaki, G. J. A systematic approach to alkaline-surfactant-foam flooding of heavy oil: microfluidic assessment with a novel phase-behavior viscosity map. *Sci. Rep.* **2020**, *10*, No. 12930.
(32) Saadat, M.; Tsai, P. A.; Ho, T.-H.; Øye, G.; Dudek, M. Development of a microfluidic method to study enhanced oil recovery by low salinity water flooding. *ACS Omega* **2020**, *5*, 17521−17530.
(33) Yun, W.; Chang, S.; Cogswell, D. A.; Eichmann, S. L.; Gizzatov, A.; Thomas, G.; Al-Hazza, N.; Abdel-Fattah, A.; Wang, W. Toward reservoir-on-a-chip: rapid performance evaluation of enhanced oil recovery surfactants for carbonate reservoirs using a calcite-coated micromodel. *Sci. Rep.* **2020**, *10*, No. 782.
(34) He, K.; Xu, L.; Gao, Y.; Yin, X.; Neeves, K. B. Evaluation of surfactant performance in fracturing fluids for enhanced well productivity in unconventional reservoirs using Rock-on-a-Chip approach. *J. Pet. Sci. Eng.* **2015**, *135*, 531−541.
(35) Tahir, M.; Hincapie, R. E.; Langanke, N.; Ganzer, L.; Jaeger, P. Coupling Microfluidics Data with Core Flooding Experiments to Understand Sulfonated/Polymer Water Injection. *Polymers* **2020**, *12*, No. 1227.
(36) Buchgraber, M.; Al-Dossary, M.; Ross, C.; Kovscek, A. R. Creation of a dual-porosity micromodel for pore-level visualization of multiphase flow. *J. Pet. Sci. Eng.* **2012**, *86*−*87*, 27−38.
(37) Yun, W.; Ross, C. M.; Roman, S.; Kovscek, A. R. Creation of a dual-porosity and dual-depth micromodel for the study of multiphase flow in complex porous media. *Lab Chip* **2017**, *17*, 1462−1474.
(38) Xu, K.; Liang, T.; Zhu, P.; Qi, P.; Lu, J.; Huh, C.; Balhoff, M. A 2.5-D glass micromodel for investigation of multi-phase flow in porous media. *Lab Chip* **2017**, *17*, 640−646.
(39) Yu, F.; Jiang, H.; Xu, F.; Fan, Z.; Su, H.; Li, J. New insights into flow physics in the EOR process based on 2.5D reservoir micromodels. *J. Pet. Sci. Eng.* **2019**, *181*, No. 106214.
(40) Krummel, A. T.; Datta, S. S.; Münster, S.; Weitz, D. A. Visualizing multiphase flow and trapped fluid configurations in a model three-dimensional porous medium. *AIChE J.* **2013**, *59*, 1022−1029.
(41) Le-Anh, D.; Rao, A.; Ayirala, S. C.; Alotaibi, M. B.; Duits, M. H.; Gardeniers, H.; Yousef, A. A.; Mugele, F. Optical measurements of oil release from calcite packed beds in microfluidic channels. *Microfluid. Nanofluid.* **2020**, *24*, No. 47.
(42) de Haas, T. W.; Fadaei, H.; Guerrero, U.; Sinton, D. Steam-on-a-chip for oil recovery: the role of alkaline additives in steam assisted gravity drainage. *Lab Chip* **2013**, *13*, 3832−3839.
(43) Argüelles-Vivas, F.; Babadagli, T. Gas (air)−heavy oil displacement in capillary media at high temperatures: A CFD approach to model microfluidics experiments. *Chem. Eng. Sci.* **2016**, *140*, 299−308.

https://doi.org/10.1021/acs.energyfuels.1c03670
Energy Fuels XXXX, XXX, XXX−XXX

(44) Bao, B.; Sanders, A.; Ren, G.; Haas, T. In *Rapid Microfluidic Analysis of Thermal Foam Stability at 250 Degrees Celsius*, Abu Dhabi International Petroleum Exhibition & Conference; OnePetro, 2017.
(45) Wegner, J.; Ganzer, L. In *Rock-on-a-Chip Devices for High p, T Conditions and Wettability Control for the Screening of EOR Chemicals*, SPE Europec featured at 79th EAGE Conference and Exhibition; OnePetro, 2017.
(46) Saadat, M.; Vikse, N. B.; Øye, G.; Dudek, M. A microfluidic study of oil displacement in porous media at elevated temperature and pressure. *Sci. Rep.* **2021**, *11*, No. 20349.
(47) Liu, Y.; Block, E.; Squier, J.; Oakey, J. Investigating low salinity waterflooding via glass micromodels with triangular pore-throat architectures. *Fuel* **2021**, *283*, No. 119264.
(48) Saadat, M.; Yang, J.; Dudek, M.; Øye, G.; Tsai, P. A. Microfluidic investigation of enhanced oil recovery: The effect of aqueous floods and network wettability. *J. Pet. Sci. Eng.* **2021**, *203*, No. 108647.
(49) Tetteh, J. T.; Cudjoe, S. E.; Aryana, S. A.; Ghahfarokhi, R. B. Investigation into fluid-fluid interaction phenomena during low salinity waterflooding using a reservoir-on-a-chip microfluidic model. *J. Pet. Sci. Eng.* **2021**, *196*, No. 108074.
(50) Collins, S.; Melrose, J. *Adsorption of Asphaltenes and Water on Reservoir Rock Minerals*, SPE Oilfield and Geothermal Chemistry Symposium; OnePetro, 1983.
(51) Buckley, J. S.; Liu, Y.; Xie, X.; Morrow, N. R. Asphaltenes and crude oil wetting-the effect of oil composition. *SPE J.* **1997**, *2*, 107−119.
(52) Pernyeszi, T.; Patzkó, Á.; Berkesi, O.; Dékány, I. Asphaltene adsorption on clays and crude oil reservoir rocks. *Colloids Surf., A* **1998**, *137*, 373−384.
(53) Marczewski, A. W.; Szymula, M. Adsorption of asphaltenes from toluene on mineral surface. *Colloids Surf., A* **2002**, *208*, 259−266.
(54) Chávez-Miyauchi, T. E.; Firoozabadi, A.; Fuller, G. G. Nonmonotonic elasticity of the crude oil−brine interface in relation to improved oil recovery. *Langmuir* **2016**, *32*, 2192−2198.
(55) Au, A. K.; Huynh, W.; Horowitz, L. F.; Folch, A. 3D-printed microfluidics. *Angew. Chem., Int. Ed.* **2016**, *55*, 3862−3881.
(56) Freer, E.; Svitova, T.; Radke, C. The role of interfacial rheology in reservoir mixed wettability. *J. Pet. Sci. Eng.* **2003**, *39*, 137−158.
(57) Ayirala, S. C.; Al-Yousef, A. A.; Li, Z.; Xu, Z. Water ion interactions at crude-oil/water interface and their implications for smart waterflooding in carbonates. *SPE J.* **2018**, *23*, 1817−1832.
(58) Zhang, S.; Zhang, L.; Lu, X.; Shi, C.; Tang, T.; Wang, X.; Huang, Q.; Zeng, H. Adsorption kinetics of asphaltenes at oil/water interface: Effects of concentration and temperature. *Fuel* **2018**, *212*, 387−394.
(59) Wensink, H.; Berenschot, J. W.; Jansen, H. V.; Elwenspoek, M. C. In *High Resolution Powder Blast Micromachining*, Proceedings IEEE Thirteenth Annual International Conference on Micro Electro Mechanical Systems (Cat. No. 00CH36308); IEEE, 2000; pp 769−774.
(60) Gunda, N. S. K.; Joseph, J.; Tamayol, A.; Akbari, M.; Mitra, S. K. Measurement of pressure drop and flow resistance in microchannels with integrated micropillars. *Microfluid. Nanofluid.* **2013**, *14*, 711−721.
(61) Jing-qiang, L.; Chao-mo, Z.; Zhansong, Z. Combine the capillary pressure curve data with the porosity to improve the prediction precision of permeability of sandstone reservoir. *J. Pet. Sci. Eng.* **2016**, *139*, 43−48.
(62) Rücker, M.; Bartels, W. B.; Singh, K.; Brussee, N.; Coorn, A.; van der Linde, H. A.; Bonnin, A.; Ott, H.; Hassanizadeh, S. M.; Blunt, M. J.; et al. The effect of mixed wettability on pore-scale flow regimes based on a flooding experiment in Ketton limestone. *Geophys. Res. Lett.* **2019**, *46*, 3225−3234.
(63) Yiotis, A.; Karadimitriou, N.; Zarikos, I.; Steeb, H. Pore-scale effects during the transition from capillary-to viscosity-dominated flow dynamics within microfluidic porous-like domains. *Sci. Rep.* **2021**, *11*, No. 3891.
(64) Gerold, C. T.; Krummel, A. T.; Henry, C. S. Microfluidic devices containing thin rock sections for oil recovery studies. *Microfluid. Nanofluid.* **2018**, *22*, No. 76.
(65) Arhuoma, M.; Yang, D.; Dong, M.; Li, H.; Idem, R. Numerical simulation of displacement mechanisms for enhancing heavy oil recovery during alkaline flooding. *Energy Fuels* **2009**, *23*, 5995−6002.
(66) Primkulov, B. K.; Pahlavan, A. A.; Fu, X.; Zhao, B.; MacMinn, C. W.; Juanes, R. Signatures of fluid−fluid displacement in porous media: wettability, patterns and pressures. *J. Fluid Mech.* **2019**, 875.
(67) Primkulov, B. K.; Pahlavan, A. A.; Fu, X.; Zhao, B.; MacMinn, C. W.; Juanes, R. Wettability and Lenormand's diagram. *J. Fluid Mech.* **2021**, 923.
(68) Lenormand, R.; Zarcone, C. Invasion percolation in an etched network: measurement of a fractal dimension. *Phys. Rev. Lett.* **1985**, *54*, 2226.
(69) Mugele, F.; Bera, B.; Cavalli, A.; Siretanu, I.; Maestro, A.; Duits, M.; Cohen-Stuart, M.; van den Ende, D.; Stocker, I.; Collins, I. Ion adsorption-induced wetting transition in oil-water-mineral systems. *Sci. Rep.* **2015**, *5*, No. 10519.
(70) Haagh, M. E. J.; Sîretanu, I.; Duits, M.; Mugele, F. Salinity-dependent contact angle alteration in oil/brine/silicate systems: the critical role of divalent cations. *Langmuir* **2017**, *33*, 3349−3357.
(71) Haagh, M. E.; Schilderink, N.; Duits, M. H.; Siretanu, I.; Mugele, F.; Collins, I. R. Salinity-dependent contact angle alteration in oil/brine/silicate systems: The effect of temperature. *J. Pet. Sci. Eng.* **2018**, *165*, 1040−1048.
(72) Nair, S.; Gao, J.; Otto, C.; Duits, M. H.; Mugele, F. In-situ observation of reactive wettability alteration using algorithm-improved confocal Raman microscopy. *J. Colloid Interface Sci.* **2021**, *584*, 551−560.
(73) Tabrizy, V. A.; Hamouda, A.; Denoyel, R. Influence of magnesium and sulfate ions on wettability alteration of calcite, quartz, and kaolinite: surface energy analysis. *Energy Fuels* **2011**, *25*, 1667−1680.
(74) Qi, Z.; Wang, Y.; He, H.; Li, D.; Xu, X. Wettability alteration of the quartz surface in the presence of metal cations. *Energy Fuels* **2013**, *27*, 7354−7359.
(75) Rao, A.; Kumar, S.; Annink, C.; Le-Anh, D.; Ayirala, S. C.; Alotaibi, M. B.; Siretanu, I.; Duits, M. H.; Yousef, A. A.; Mugele, F. Mineral Interfaces and Oil Recovery: A Microscopic View on Surface Reconstruction, Organic Modification, and Wettability Alteration of Carbonates. *Energy Fuels* **2020**, *34*, 5611−5622.
(76) Rao, A.; Kumar, S.; Annink, C.; Le-Anh, D.; B Alotaibi, M.; C Ayirala, S.; Siretanu, I.; Duits, M.; Mugele, F.; A Yousef, A. In *Artificial Diagenesis of Carbonates: Temperature Dependent Inorganic and Organic Modifications in Reservoir Mimetic Fluids*, SPE Improved Oil Recovery Conference; OnePetro, 2020.
(77) Acevedo, S.; Castillo, J.; Fernández, A.; Goncalves, S.; Ranaudo, M. A. A study of multilayer adsorption of asphaltenes on glass surfaces by photothermal surface deformation. Relation of this adsorption to aggregate formation in solution. *Energy Fuels* **1998**, *12*, 386−390.
(78) Castillo, J.; Goncalves, S.; Fernández, A.; Mujica, V. Applications of photothermal displacement spectroscopy to the study of asphaltenes adsorption. *Opt. Commun.* **1998**, *145*, 69−75.
(79) Labrador, H.; Fernández, Y.; Tovar, J.; Munoz, R.; Pereira, J. C. Ellipsometry study of the adsorption of asphaltene films on a glass surface. *Energy Fuels* **2007**, *21*, 1226−1230.
(80) Adams, J. J. Asphaltene adsorption, a literature review. *Energy Fuels* **2014**, *28*, 2831−2856.
(81) Haagh, M. E.; Schilderink, N.; Mugele, F.; Duits, M. H. Wetting of mineral surfaces by fatty-acid-laden oil and brine: carbonate effect at elevated temperature. *Energy Fuels* **2019**, *33*, 9446−9456.
(82) He, W.; Chen, K.; Hayatdavoudi, A.; Sawant, K.; Lomas, M. Effects of clay content, cement and mineral composition characteristics on sandstone rock strength and deformability behaviors. *J. Pet. Sci. Eng.* **2019**, *176*, 962−969.
(83) Iyi, D.; Balogun, Y.; Oyeneyin, B.; Faisal, N. Numerical modelling of the effect of wettability, interfacial tension and

https://doi.org/10.1021/acs.energyfuels.1c03670
Energy Fuels XXXX, XXX, XXX−XXX

temperature on oil recovery at pore-scale level. *J. Pet. Sci. Eng.* **2021**, *201*, No. 108453.
(84) Mahzari, P.; Sohrabi, M.; Cooke, A. J.; Carnegie, A. Direct pore-scale visualization of interactions between different crude oils and low salinity brine. *J. Pet. Sci. Eng.* **2018**, *166*, 73−84.
(85) Dangerfield, J.; Brown, D. *The Ekofi Sk Field: North Sea Oil and Gas Reservoirs*, Kleepe, L. J., Eds.; Graharm and Trotman, 1987.
(86) Tang, G.; Morrow, N. R. Salinity, temperature, oil composition, and oil recovery by waterflooding. *SPE Reservoir Eng.* **1997**, *12*, 269−276.
(87) Donaldson, E. C.; Alam, W. *Wettability*; Elsevier, 2013.
(88) Han, B.-B.; Cheng, W.-L.; Nian, Y.-L. Experimental study on effect of temperature field on recovery of reservoir using hot water flooding. *Energy Procedia* **2017**, *142*, 3759−3765.
(89) Barnaji, M. J.; Pourafshary, P.; Rasaie, M. R. Visual investigation of the effects of clay minerals on enhancement of oil recovery by low salinity water flooding. *Fuel* **2016**, *184*, 826−835.
(90) Sharifipour, M.; Pourafshary, P.; Nakhaee, A. Study of the effect of clay swelling on the oil recovery factor in porous media using a glass micromodel. *Appl. Clay Sci.* **2017**, *141*, 125−131.

https://doi.org/10.1021/acs.energyfuels.1c03670
Energy Fuels XXXX, XXX, XXX−XXX